Design and Optimization of an Electric Vehicle Wireless Charging System Using Interleaved Boost Converter and Flat Solenoid Coupler

Yousu Yao, *Member, IEEE*, Shenghan Gao, Yijie Wang, *Senior Member, IEEE*, Xiaosheng Liu, *Member, IEEE*, Xiangjun Zhang, and Dianguo Xu, *Fellow, IEEE*

***Abstract*—Simple but effective output voltage/current control schemes are essential for electric vehicle wireless charging systems (EVWCSs). This article proposes an EVWCS using interleaved boost converter (IBC) and flat solenoid coupler (FSC). The closed-loop control between the primary and secondary is realized by adjusting the duty cycle of the IBC. The currents and losses in the primary are reduced in the proposed system because the dc bus voltage in the primary is increased by using the IBC. The input current ripple is diminished owing to the interleaved structure. This article also proposes a parameter optimization method to obtain the optimal FSC. Without loss of generality, the total area of the transmitter (Tx) and receiver (Rx) is assumed to be constant, and the Tx is assumed to be larger than the Rx. A scale-down prototype whose output power is 500 W was built in the laboratory to verify the theoretical analysis. The output voltage of the prototype kept constant when the misalignment was 200 mm in the winding direction or 100 mm in the magnetic direction. A highest system efficiency, from dc input to dc output, of 90.1% was achieved when the power transfer distance was 170 mm.**

***Index Terms*—Closed-loop control, flat solenoid coupler (FSC), interleaved boost converter (IBC), parameter optimization, wireless charging system.**

I. Introduction

WIRELESS power transfer (WPT) can transmit electrical energy through a relatively large air gap. It shows the advantages of flexibility, convenience, and safety. Most of the disadvantages of conductive power transfer can be overcome or diminished by using this new technology [1]–[3]. WPT can be employed in many applications such as electric vehicles, automatic underwater vehicles, and implantable medical devices [4]–[6].

To expand the load lifetime and achieve better performance, the output voltage/current of a WPT system should be stable. Nevertheless, the misalignment between the transmitter (Tx) and receiver (Rx) has great impact on output voltage/current. Hence, an effective closed-loop control scheme is essential. Three types of control strategies are commonly utilized in WPT systems. They are primary side control (PSC), secondary side control (SSC), and primary and secondary sides control (PSSC), respectively [7]–[10]. In this article, PSC (SSC) refers to the control that both the sampling and control are implemented at the primary (secondary) side, while PSSC refers to the control that the sampling and control are implemented at the secondary and primary sides, respectively. The response of PSC is fast, but the output accuracy is low. It is not suitable for the scenarios where high output accuracy is required. The output accuracy of SSC is high, but it increases the volume and weight of the Rx. PSSC feeds the output voltage/current at the secondary back to the primary. Hence, the control accuracy is high. In addition, PSSC is suitable for the applications where the primary space is large and the secondary space is small, for instance, the electric vehicle wireless charging systems (EVWCSs). Therefore, this article will focus on PSSC.

Variable frequency control at the primary and secondary sides can keep the output voltage/current constant, but it results in the loss of resonance and zero phase angle (ZPA), and introduces a large amount of reactive power increasing the stresses over the components [9]. Phase shift control of a WPT system using a full-bridge inverter (FBI) can maintain the resonance of the system, but the disadvantages of low inverter gain (defined as the ratio of the fundamental harmonic of the output voltage of the inverter to the dc input voltage of the inverter) and narrow adjustment range limit its utilization in practical systems [10]. To increase the inverter gain and widen the adjustment range, this article replaces the FBI with an interleaved boost converter (IBC). A greater inverter gain indicates a higher output voltage of the inverter and smaller currents and losses in the primary. Moreover, IBC can reduce the ripple of the dc input current. Consequently, the impact of the WPT system on power grid is attenuated.

Misalignment tolerance is an important issue in EVWCSs. Optimizing compensation topologies and modifying magnetic couplers are two widely employed methods which can effectively improve the misalignment tolerance of WPT systems. However, optimizing compensation topologies may introduce additional resonant components and reduce system efficiency

Manuscript received February 29, 2020; revised June 29, 2020; accepted August 16, 2020. Date of publication August 25, 2020; date of current version November 20, 2020. This work was supported by the Fundamental Research Funds for the Central Universities. Recommended for publication by Associate Editor C. Fernandez. *(Corresponding author: Yousu Yao.)*

The authors are with the School of Electrical Engineering and Automation, Harbin Institute of Technology, Harbin 150001, China (e-mail: yaoyousu@163.com; hitgsh@163.com; wangyijie@hit.edu.cn; liuxsh@hit.edu.cn; xiangjunzh@hit.edu.cn; xudiang@hit.edu.cn).

Color versions of one or more of the figures in this article are available online at https://ieeexplore.ieee.org.

Digital Object Identifier 10.1109/TPEL.2020.3019441

[11]–[15]. Therefore, the misalignment tolerance will be improved by modifying magnetic couplers in this article.

Flat solenoid coupler (FSC) provides good misalignment tolerance in winding direction but poor misalignment tolerance in magnetic direction. To reduce the cost and weight, H-shaped and split-core-based FSCs were proposed where the amount of the ferrite core was significantly decreased [16]–[21]. To improve the coupling coefficient and misalignment tolerance of FSCs, the ferrite shape was carefully optimized [22], [23]. Moreover, some researchers combine FSCs with other couplers to make full use of the advantages of different magnetic couplers [24].

Although a lot of studies have been done to improve the performance of FSCs, some issues need to be further addressed. For example, is H-shaped core the optimal? How many segments should the core be split into for a split-core-based FSC? How much ferrite can be taken out from the original core? This article proposes a parameter design method based on which the optimal FSC employing much less ferrite, providing sufficient coupling in the whole operating area, and showing good misalignment tolerance can be readily obtained. Considering the wireless charging of sport utility vehicles, the power transfer distance is determined as 170 mm in this article. The maximum misalignments are 200 mm in the winding direction and 100 mm in the magnetic direction, which are 100% and 33.3% larger than the recommended values in J2954.

This article mainly has two contributions. First, introduction of the IBC into WPT system results in smaller receiver size, higher system efficiency, and lower input current ripple. The output voltage of the proposed WPT system can be regulated by changing the duty cycle of the IBC. Hence, the dc–dc converter employed in the secondary side of a conventional WPT system is removed. The receiver becomes smaller and lighter. The system efficiency is improved because the dc bus voltage is boosted, and the currents in the primary side are reduced. The input current ripple becomes much lower owing to the interleaved structure. It significantly reduces the impact of the WPT system on power grid. Second, a novel magnetic coupler based on flat solenoid coil is proposed for electric vehicle wireless charging. The proposed coupler shows the advantages of higher coupling coefficient, better misalignment tolerance, and less ferrite core usage.

The remainder of this article is organized as follows. Section II analyzes the working principles of the proposed EVWCS, especially the input and output characteristics of the IBC. Section III introduces the proposed parameter design method in detail. Section IV focuses on the system modeling and closed-loop control strategy. To verify the correctness of the theoretical analysis and the advantages of the proposed system, a prototype whose output power is 500 W was built in Section V. Finally, Section VI concludes the article.

II. Circuit Analysis of the Proposed EVWCS

A. Introduction of the Proposed System

Fig. 1 shows the schematic circuit of the proposed EVWCS. $U_{\rm in}$ is the dc input voltage. $C_{\rm in}$ is the voltage-stabilizing capacitor. $U_{\rm Cin}$ is termed dc bus voltage in this article. L_1 and

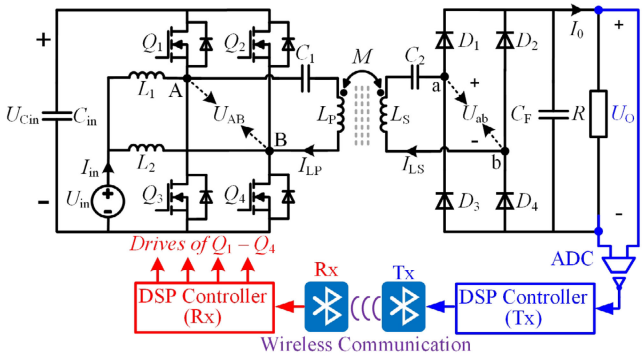

Fig. 1. Schematic circuit of the proposed EVWCS.

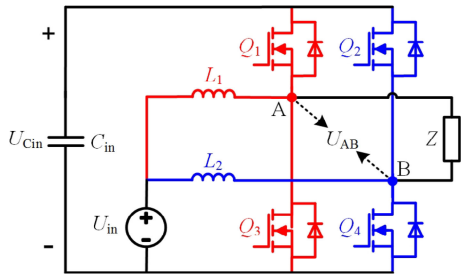

Fig. 2. Schematic circuit of the boost inverter.

L_2 are two interleaved inductors. Q_1–Q_4 are four MOSFETs. L_1, L_2, and Q_1–Q_4 constitute the IBC. It works as not only a boost converter which boosts $U_{\rm in}$ to $U_{\rm Cin}$ but also a FBI which converts $U_{\rm Cin}$ into the high-frequency square-wave voltage $U_{\rm AB}$. For the sake of straightforwardness, it is called boost inverter hereafter. C_1 and C_2 are the primary and secondary series compensation capacitors, respectively. $L_{\rm P}$ and $L_{\rm S}$ are the primary and secondary self-inductances of the magnetic coupler, while M is the mutual inductance, D_1–D_4 are four diodes, $C_{\rm F}$ is the filtering capacitor, and R is the resistive load. The output voltage $U_{\rm O}$ is sampled in the secondary and then transmitted to the primary using Bluetooth HC-05. The received output voltage is compared with the preset value. The difference between them is sent to the PID controller to control the ON and OFF of the MOSFETs and keep the output voltage constant in the case of misalignment.

B. Output Characteristics of the Boost Inverter

Fig. 2 shows the schematic circuit of the boost inverter. Z stands for the equivalent impedance of the poststage circuit. L_1, Q_1, and Q_3 constitute the first boost converter. L_2, Q_2, and Q_4 constitute the second boost converter. Similar to the duty cycle of a boost converter, the ratio of the ON time of Q_3 and Q_4 to the whole period is defined as the duty cycle D for the boost inverter. The ON time of Q_3 equals to that of Q_4 but Q_4 lags Q_3 by half period. The conduction of Q_1 and Q_3 as well as Q_2 and Q_4 is complementary.

The duty cycle of the boost inverter can be categorized into three cases, i.e., $D < 0.5$, $D = 0.5$, and $D > 0.5$. L_1, and L_2 are

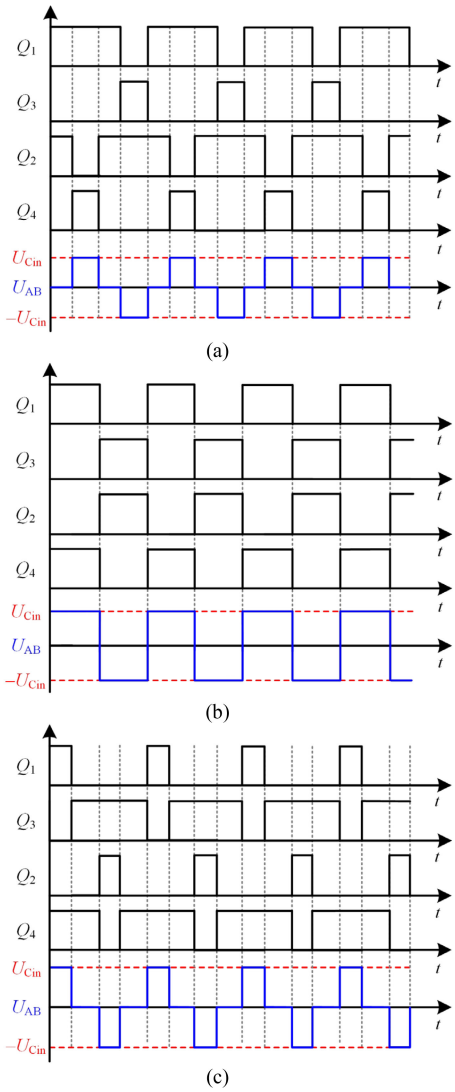

Fig. 3. Drive signals of Q_1–Q_4 and waveforms of U_{AB} with different duty cycles. (a) $D < 0.5$. (b) $D = 0.5$. (c) $D > 0.5$.

alternately charged and discharged throughout the operation, resulting in a stable U_{Cin}, which is assumed to be constant in the analysis. Based on the principle of volt–second balance, the following equation can be deduced

$$U_{in}DT + (U_{in} - U_{Cin})(1 - D)T = 0. \tag{1}$$

Then, U_{Cin} is obtained by solving (1)

$$U_{Cin} = \frac{U_{in}}{1 - D}. \tag{2}$$

Fig. 3 shows the drive signals of Q_1–Q_4 and waveforms of U_{AB} in the cases of different duty cycles. θ_{dead} represents the dead angle of U_{AB}, which can be expressed as follows:

$$\theta_{dead} = \begin{cases} \pi - 2\pi D & (D < 0.5) \\ 0 & (D = 0.5) \\ 2\pi D - \pi & (D > 0.5). \end{cases} \tag{3}$$

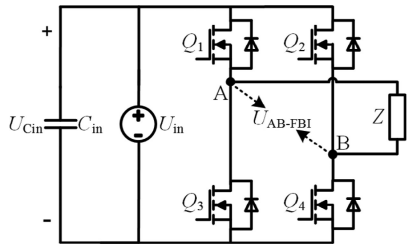

Fig. 4. Schematic circuit of a conventional full-bridge inverter.

According to the Fourier decomposition, the root mean square (rms) of the fundamental harmonic of U_{AB} can be yielded

$$U_{AB1} = \begin{cases} \frac{2\sqrt{2}U_{in}}{\pi(1-D)} \cos\left(\frac{\pi}{2} - \pi D\right) & (D < 0.5) \\ \frac{4\sqrt{2}}{\pi} U_{in} & (D = 0.5) \\ \frac{2\sqrt{2}U_{in}}{\pi(1-D)} \cos\left(\pi D - \frac{\pi}{2}\right) & (D > 0.5). \end{cases} \tag{4}$$

Equation (4) can be simplified into

$$U_{AB1} = \frac{2\sqrt{2}U_{in}}{\pi(1 - D)} \cos\left(\pi D - \frac{\pi}{2}\right) \quad (0 < D < 1). \tag{5}$$

Based on the definition of the inverter gain, it can be deduced as follows:

$$G_{BI} = \frac{U_{AB1}}{U_{in}} = \frac{2\sqrt{2}}{\pi(1 - D)} \cos\left(\pi D - \frac{\pi}{2}\right). \tag{6}$$

Fig. 4 shows the schematic circuit of a conventional FBI. $U_{AB\text{-}FBI}$ represents the output voltage of the FBI. The fundamental harmonic of $U_{AB\text{-}FBI}$ (rms value) can be calculated using the following equation when the phase shift angle is 0:

$$U_{AB1-FBI} = \frac{2\sqrt{2}}{\pi} U_{in}. \tag{7}$$

The inverter gain of the FBI can be derived

$$G_{FBI} = \frac{U_{AB1-FBI}}{U_{in}} = \frac{2\sqrt{2}}{\pi}. \tag{8}$$

A novel parameter G_0, defined as the ratio of G_{BI} to G_{FBI}, is introduced to compare the inverter gain of the BI and FBI

$$G_0 = \frac{G_{BI}}{G_{FBI}} = \frac{1}{1 - D} \cos\left(\pi D - \frac{\pi}{2}\right). \tag{9}$$

On the basis of (2), the ratio of U_{Cin} to U_{in}, termed boost ratio in this article, can be obtained

$$G_{BR} = \frac{U_{Cin}}{U_{in}} = \frac{1}{1 - D}. \tag{10}$$

Fig. 5 shows the plots of G_0 and G_{BR} as functions of the duty cycle. When D is smaller than 0.27, the dead time of U_{AB} is relatively long and G_0 is lower than 1. When D is greater than 0.67, G_{BR} is higher than 3 and U_{Cin} is quite high. The MOSFETs with high drain-to-source voltages should be selected, which increases system cost and deteriorates system reliability. Therefore, D is determined to be higher than 0.27 and lower than 0.67 in the proposed system.

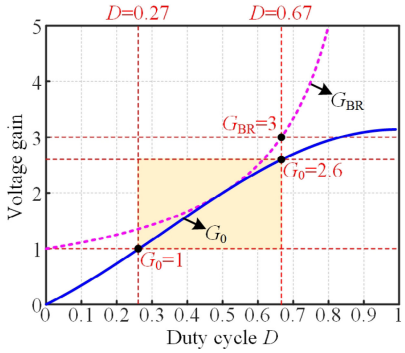

Fig. 5. Plots of G_0 and G_{BR} as functions of the duty cycle D.

C. Advantages of the Boost Inverter

The transmitter of an EVWCS is usually large in size, and the number of turns is great. Hence, the equivalent series resistance (ESR) of the transmitter is high. Reducing the current flowing through the transmitter can effectively reduce the loss and improve system efficiency. The boost inverter can step up the dc bus voltage and lower the current flowing through the transmitter. In other words, the boost inverter can improve system efficiency by decreasing the loss of the transmitter.

The voltage-stabilizing capacitor C_{in} of the FBI (see Fig. 4) is periodically charged and discharged, causing a large ripple in the input current. The input current ripple has great impact on the power grid. This problem can be alleviated when a BI is employed. Fig. 6 shows the input current (I_{in}) and inductor currents (I_{L1} and I_{L2}) of a BI in the cases of different duty cycles. I_{in} equals the sum of I_{L1} and I_{L2}. Owing to the interleaved structure, the ripples of I_{L1} and I_{L2} cancel each other out. Hence, the ripple of I_{in} is small. It is even zero when the duty cycle is 0.5.

D. Output Characteristics of the Proposed EVWCS

SS compensation topology showing many advantages including ZPA, high efficiency, good high-order harmonics suppression capability, and coupling-independent resonant frequency is employed in this article. To minimize power loss and achieve ZPA, C_1 (C_2) should resonate with L_{P} (L_{S}) at system operating frequency f_0

$$\omega_0{}^2 = (2\pi f_0)^2 = \frac{1}{C_1 L_{\mathrm{P}}} = \frac{1}{C_2 L_{\mathrm{S}}}. \tag{11}$$

ω_0 is system operating angular frequency. Equation (12) gives the correlation between U_{O} and U_{in}. The duty cycle D will be adjusted to keep U_{O} constant if a misalignment appears. R_{N} is the nominal resistance

$$U_{\mathrm{O}} = \frac{8R_{\mathrm{N}} \cos\left(\pi D - \frac{\pi}{2}\right) U_{\mathrm{in}}}{\pi^2 (1-D)\, k\omega_0 \sqrt{L_{\mathrm{P}} L_{\mathrm{S}}}}. \tag{12}$$

III. Optimization of the Flat Solenoid Coupler

The transmitter embedded in the ground is generally larger than the receiver mounted on the vehicle due to the size limitation of the chassis in an EVWCS. Fig. 7 shows the original FSC for

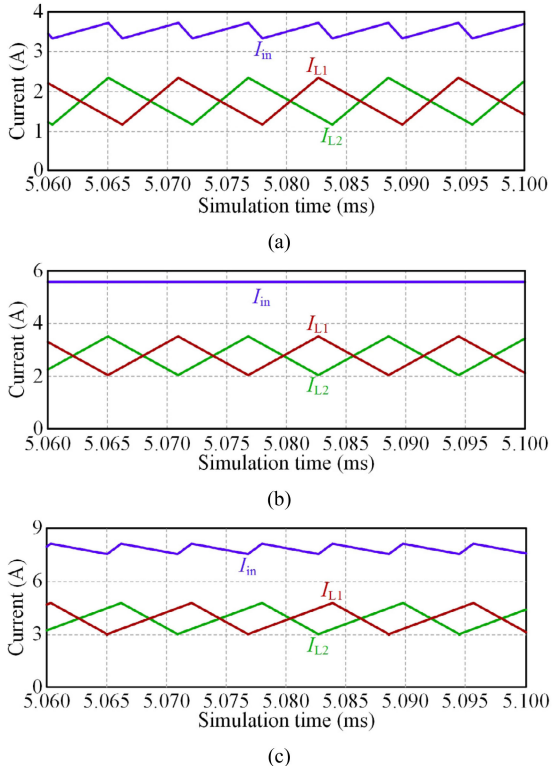

Fig. 6. Simulation results of the input current (I_{in}) and inductor currents (I_{L1} and I_{L2}) of a BI. (a) $D < 0.5$. (b) $D = 0.5$. (c) $D > 0.5$.

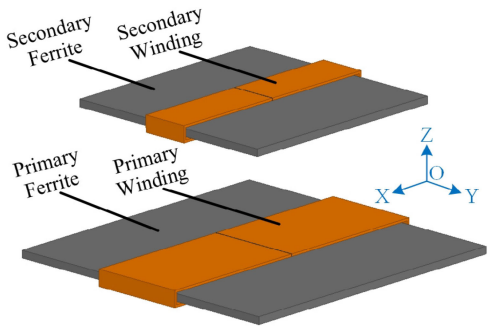

Fig. 7. Original FSC for EVWCSs.

EVWCSs which has not been optimized. It is comprised of two ferrites and two windings.

Fig. 8 shows the main size parameters of the original FSC. The power transfer distance from the upper surface of the transmitter to the lower surface of the receiver is D_{PT}. L_{PF} and W_{PF} (L_{SF} and W_{SF}) represent the length and width of the primary (secondary) ferrite. C_{WF} stands for the clearance between the winding and ferrite. It is 3 mm because the ferrite is placed in a cuboid acrylic box whose thickness is 3 mm. The thickness of winding (ferrite) is represented by T_{W} (T_{F}). W_{PW} and W_{SW} are the widths of the primary and secondary windings, respectively.

Among the aforementioned size parameters, L_{SF}, L_{PF}, W_{SF}, W_{PF}, D_{PT}, W_{SW}, and W_{PW} are determined by the applications. They are unchanged in this article. The impact of T_{F}, T_{W},

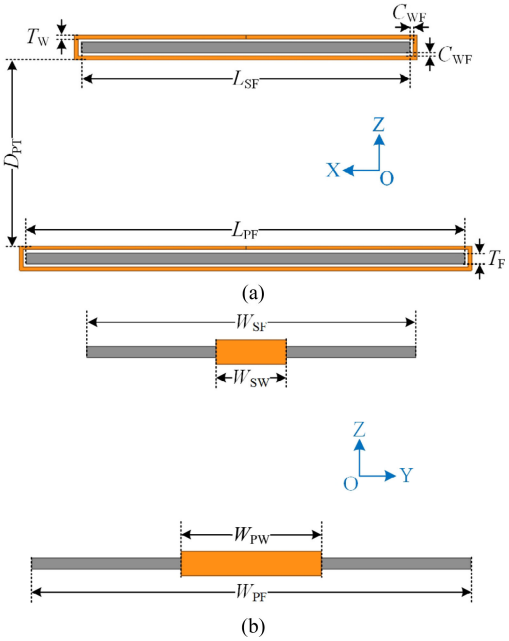

Fig. 8. Main size parameters of the original FSC. (a) Right and (b) front views.

TABLE I
UNCHANGED SIZE PARAMETERS UTILIZED IN THE SIMULATIONS

Parameter	Value	Parameter	Value
L_{SF}	300 mm	W_{SW}	64 mm
L_{PF}	400 mm	W_{PW}	128 mm
W_{SF}	300mm	T_F	10 mm
W_{PF}	400 mm	T_W	3.2 mm
D_{PT}	170 mm	C_{WF}	3 mm

and C_{WF} on coupling and misalignment tolerance is negligible because their variation ranges are small. The unchanged size parameters utilized in the simulations are listed in Table I.

The original FSC shown in Fig. 7 is cumbersome since it requires a large quantity of ferrite. The lightweight design makes great sense for the wide deployment of this coupler. In this article, a predetermined ratio of ferrite will be removed from the original coupler. This results in two issues—what is the optimal core shape and how to allocate the removed ferrite between the transmitter and receiver. These two issues will be discussed in the following two subsections, respectively. Poor misalignment tolerance in *Y* direction is another disadvantage of FSC. This article will improve the *Y*-direction misalignment tolerance of FSC by separating the windings. Both the primary and secondary windings will be divided into two subwindings connected in series. The two subwindings of the primary or secondary winding will be wound in the ferrite with a gap. The length of the gap will be optimized in subsection C. To summarize, the optimization of the FSC mainly contains three steps. The first step is to determine the primary and secondary core shapes. The second step is to obtain the optimal ratios of the removed ferrite between the transmitter and receiver. The last step is to optimize the length of the gap between two subwindings

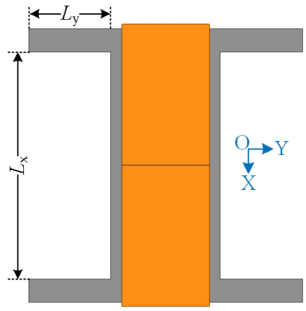

Fig. 9. Diagram of the preliminary transmitter optimization.

in both the primary and secondary sides. More details regarding the optimization can be found in the following three subsections.

A. Preliminary Optimization—Determination of Core Shape

The transmitter is first optimized. Fig. 9 shows the diagram of the preliminary transmitter optimization. L_{x} and L_{y} represent the length and width of the ferrite that is removed from the original square ferrite. To obtain a transmitter performing symmetrically with respect to *X* and *Y* axes, the removed ferrite is also symmetrical with respect to *X* and *Y* axes.

The area of the original primary ferrite is

$$S_{\mathrm{P}} = L_{\mathrm{PF}} W_{\mathrm{PF}}. \tag{13}$$

The area of the removed ferrite is

$$S_{\mathrm{RP}} = 2L_{\mathrm{x}}L_{\mathrm{y}} = k_1 S_{\mathrm{P}} \tag{14}$$

where k_1 is the ratio of S_{RP} to S_{P}. It is determined as 50% in this article. The variation ranges of L_{x} and L_{y} (constraints of the preliminary transmitter optimization) can be readily obtained from Fig. 9

$$\begin{cases} 0 \le L_{\mathrm{x}} \le L_{\mathrm{PF}} \\ 0 \le L_{\mathrm{y}} \le \frac{W_{\mathrm{PF}}}{2} \end{cases}. \tag{15}$$

Substituting the parameters in Table I into (13)–(15), the variation range of L_{y}, 100 mm $\le L_{\mathrm{y}} \le$ 200 mm, can be obtained. Fig. 10 shows the coupling coefficients as functions of *X*- and *Y*-axis misalignments and L_{y}. $\mathrm{CRR}_{\Delta X}$ and $\mathrm{CRR}_{\Delta Y}$ represent the coupling retaining ratios in *X* and *Y* directions. They are defined by (16), where $k_{\Delta X}$, $k_{\Delta Y}$, and k_{ali} stand for the coupling coefficients under misaligned and aligned cases, respectively. The subscripts $\Delta X = 200$ and $\Delta Y = 100$ imply that the misalignments in *X* and *Y* directions are 200 and 100 mm, respectively. $\mathrm{CRR}_{\Delta X}$ and $\mathrm{CRR}_{\Delta Y}$ are indicators reflecting the misalignment tolerance of a magnetic coupler

$$\mathrm{CRR}_{\Delta X} = \frac{k_{\Delta X}}{k_{\mathrm{ali}}}, \quad \mathrm{CRR}_{\Delta Y} = \frac{k_{\Delta Y}}{k_{\mathrm{ali}}}. \tag{16}$$

As shown in Fig. 10(a), the coupling coefficient increases gradually, whereas $\mathrm{CRR}_{\Delta X\,=\,200}$ increases first and decreases later as L_y increases from 100 to 200 mm. Nevertheless, the change of $\mathrm{CRR}_{\Delta X\,=\,200}$ is so tiny that can be ignored when L_y

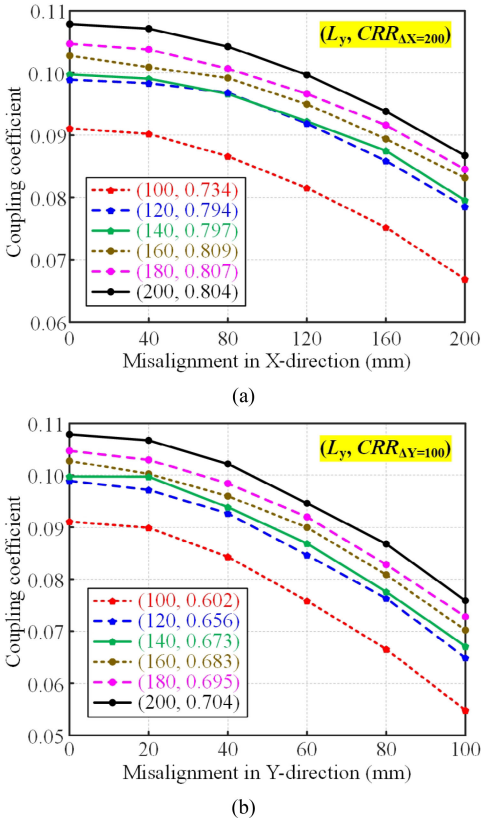

Fig. 10. Coupling coefficients as functions of (a) *X*- and (b) *Y*-direction misalignments and L_y.

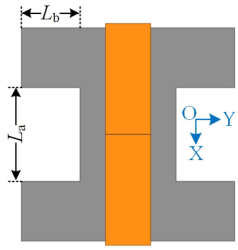

Fig. 11. Diagram of the preliminary receiver optimization.

is relatively large. As shown in Fig. 10(b), both the coupling coefficient and $\mathrm{CRR}_{\Delta Y} = 100$ increases gradually as L_y increases from 100 to 200 mm. Therefore, L_y is determined as 200 mm to acquire the highest coupling coefficient and good misalignment tolerance.

The receiver is then optimized. The preliminary optimization of the receiver is highly similar to that of the transmitter. Fig. 11 shows the diagram of the preliminary receiver optimization. L_a and L_b represent the length and width of the removed ferrite, respectively. The area of the original secondary ferrite is

$$S_\mathrm{S} = L_\mathrm{SF} W_\mathrm{SF}. \tag{17}$$

The area of the removed ferrite is

$$S_\mathrm{RS} = 2L_\mathrm{a}L_\mathrm{b} = k_2 S_\mathrm{S} \tag{18}$$

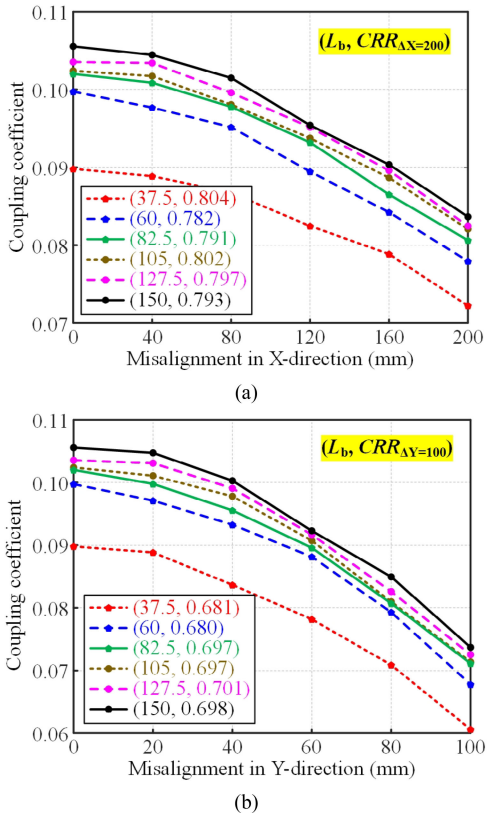

Fig. 12. Coupling coefficients as functions of (a) *X*- and (b) *Y*-direction misalignments and L_b.

where k_2 is the ratio of S_RS to S_S. It is determined as 25% in this article. The variation ranges of L_a and L_b (constraints of the preliminary transmitter optimization) are

$$\begin{cases} 0 \le L_\mathrm{a} \le L_\mathrm{SF} \\ 0 \le L_\mathrm{b} \le \frac{W_\mathrm{SF}}{2}. \end{cases} \tag{19}$$

Substituting the parameters in Table I into (17)–(19), the variation range of L_b, 37.5 mm $\le L_b \le$ 150 mm can be obtained.

Fig. 12 shows the coupling coefficients as functions of *X*- and *Y*-direction misalignments and L_b. As shown in Fig. 12(a), the coupling coefficient increases gradually and $\mathrm{CRR}_{\Delta X\,=\,200}$ fluctuates as L_b increases from 37.5 to 150 mm. The coupling coefficient is too low to transfer sufficient power when L_b is 37.5 mm even though $\mathrm{CRR}_{\Delta X\,=\,200}$ is the highest in this case. As shown in Fig. 12(b), the coupling coefficient increases gradually and $\mathrm{CRR}_{\Delta Y\,=\,100}$ increases first and decreases later as L_b increases from 37.5 to 150 mm. It is important to note that the change of $\mathrm{CRR}_{\Delta X\,=\,200}$ and $\mathrm{CRR}_{\Delta Y\,=\,100}$ in both cases is so small that can be ignored. Therefore, L_b is determined as 150 mm to obtain the highest coupling coefficient and good misalignment tolerance.

L_y equals 200 mm indicates that the optimal primary ferrite is not an H-shaped core because the intermediate ferrite has been totally removed. The preliminary optimized core of the transmitter looks like an equal sign, as shown in Fig. 13(a). For statement convenience, it is termed double-I-shaped core. The optimization of the receiver shows a similar result. The

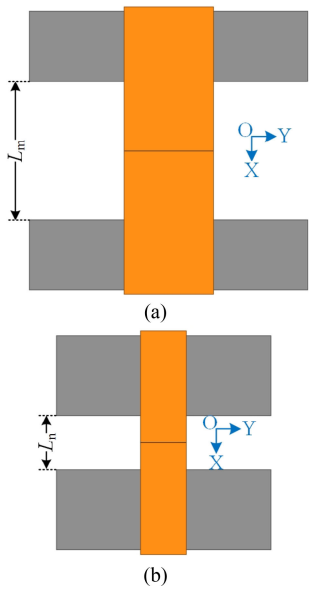

Fig. 13. Diagram of the FSC after the preliminary optimization. (a) Transmitter. (b) Receiver.

preliminary optimized core of the receiver also looks like an equal sign, as shown in Fig. 13(b). In fact, the object of the preliminary optimization is to obtain the optimal core shape. This step can be directly skipped in subsequent optimizations.

B. Second Optimization—Distribution of Removed Ferrite

The preliminary optimization determines the core shapes of the transmitter and receiver. The second optimization will distribute the removed ferrite to the transmitter and receiver with reasonable allotments in the case that the total removed ferrite is predetermined.

As shown in Fig. 13, L_m and L_n represent the lengths of the ferrites removed from the transmitter and receiver, respectively. The second optimization is based on the preliminary optimization. Hence, the volume of the removed ferrite keeps constant, i.e.,

$$L_m W_{PF} + L_n W_{SF} = k_1 S_P + k_2 S_S. \tag{20}$$

Apparently, the variation ranges of L_m and L_n (constraints of the second optimization) are

$$\begin{cases} 0 < L_m < L_{PF} \\ 0 < L_n < L_{SF}. \end{cases} \tag{21}$$

Substituting the parameters in Table I into (20) and (21), the variation range of L_m, 31.25 mm $< L_m <$ 256.25 mm, can be acquired. If L_m is very large or very small, the transmitter core or the receiver core will be very small, and the coupling coefficient will be quite low. Therefore, the lower boundary of L_m is increased to 40 mm and the upper boundary is dropped to 240 mm.

Fig. 14 shows the coupling coefficients as functions of *X*- and *Y*-direction misalignments and L_m. Although $\mathrm{CRR}_{\Delta X=200}$ and $\mathrm{CRR}_{\Delta Y=100}$ reach their peaks when L_m equals 240 mm, the coupling coefficients are quite low. This is unacceptable in practical applications because the system efficiency will be very low. The coupling coefficients when L_m equals 160 mm are similar to those when L_m equals 200 mm. However, $\mathrm{CRR}_{\Delta X=200}$ and $\mathrm{CRR}_{\Delta Y=100}$ are higher when L_m equals 200 mm. Therefore, L_m is finally determined as 200 mm.

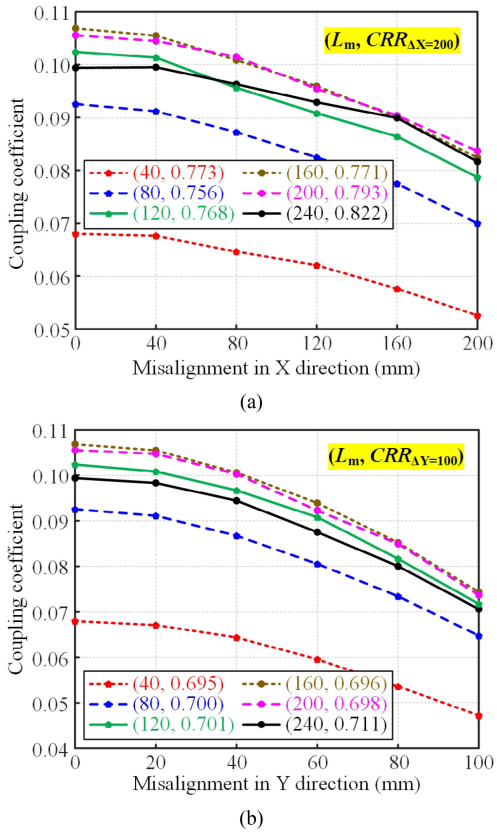

Fig. 14. Coupling coefficients as functions of (a) *X*- and (b) *Y*-direction misalignments and L_m.

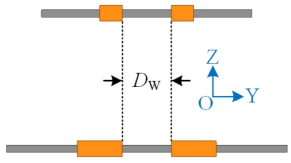

Fig. 15. Diagram of the FSC in the final optimization.

C. Final Optimization—Distances Between Separated Windings

The second optimization determines the dimensions of the cores. The final optimization will further optimize the coupling coefficient by separating the windings of the transmitter and receiver. Fig. 15 shows the diagram of the FSC in the final optimization. D_W represents the distance between the separated windings.

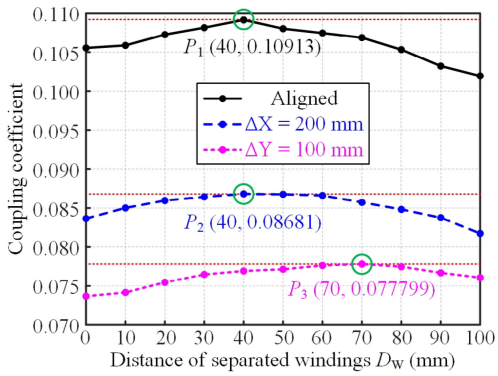

Fig. 16. Coupling coefficients as functions of D_W in aligned and misaligned cases. Two misalignments, $\Delta X = 200$ mm and $\Delta Y = 100$ mm, are considered.

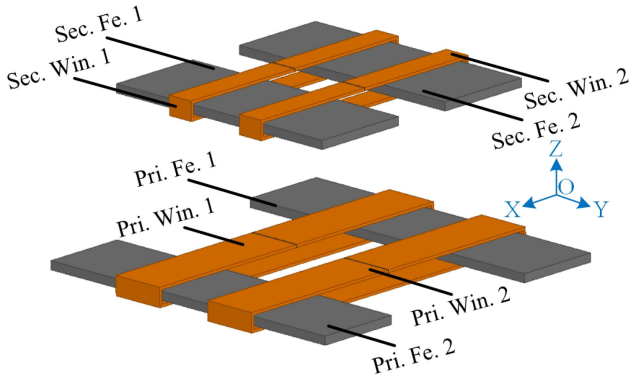

Fig. 17. Schematic of the final FSC after three times optimization where Pri., Sec., Fe., and Win. are abbreviated for Primary, Secondary, Ferrite, and Winding, respectively.

Changing the distance between the separated windings has little impact on misalignment tolerance. As a result, only the coupling coefficients are considered in the final optimization. Fig. 16 shows the coupling coefficients in three cases when D_W increases from 0 to 100 mm (constraint of the final optimization). All the three cases have their own peak points. Choosing which peak point depends on the practical requirements. In this article, the coupling coefficient is relatively low when the *Y*-direction misalignment is 100 mm. To obtain a higher coupling coefficient when $\Delta Y = 100$ mm, P_3 is chosen, i.e., $D_W = 70$ mm.

The finally obtained FSC after three optimizations is shown in Fig. 17. Both the transmitter and receiver are comprised of two parallel placed ferrite bars and two separated windings which are connected in series.

D. Comparison Between the Proposed and Conventional Couplers

Table II shows the comparison between the proposed and conventional magnetic couplers under the condition of equal ferrite size, number of turns, and power transfer distance. The magnetic couplers involved in the comparison include the planar circular, planar square, double-D (DD) and proposed structures. PS and SS represent the primary and secondary sides, respectively. PTD stands for power transfer distance. The numbers of turns of the transmitter and receiver are, respectively, 40 and 20 for all couplers. The coupling coefficients of DD coupler in all cases are low. Hence, it is not suitable for applications where the receiver is much smaller than the transmitter. Although k_{ali} of the proposed coupler is a little lower than that of the planar circular and square couplers, $CRR_{\Delta X\ =\ 200}$ and $CRR_{\Delta Y\ =\ 100}$ of the proposed coupler are much higher. In other words, the proposed coupler provides much better misalignment tolerance. Moreover, k_{ali} of the proposed coupler is 0.1069, which is sufficiently high for the transfer of electrical power with a high efficiency.

IV. System Modeling and Closed-Loop Control Strategy

Generalized state space averaging method is employed in this article to build the small signal model of the proposed EVWCS, based on which the closed-loop control characteristics are analyzed.

A. Small Signal Model of the EVWCS

Fig. 18 shows the equivalent circuit of the proposed system. g_{Q1} and g_{Q2} are the switching functions of Q_1 and Q_2 which describe the nonlinear characteristics of the boost inverter. g_D is the switching function of the rectifier which describes the nonlinear characteristics of the rectifier.

On the basis of Fig. 18, the differential equations of the proposed system can be yielded as follows:

$$\begin{cases} L_1 \frac{dI_{L1}(t)}{dt} = U_{in} - g_{Q1}(t) U_{Cin}(t) \\ L_2 \frac{dI_{L2}(t)}{dt} = U_{in} - g_{Q2}(t) U_{Cin}(t) \\ C_{in} \frac{dU_{Cin}(t)}{dt} = g_{Q1}(t) [I_{L1}(t) - I_{Lp}(t)] + \cdots \\ \qquad g_{Q2}(t) [I_{L2}(t) + I_{Lp}(t)] \\ U_{Cin}(t) [g_{Q1}(t) - g_{Q2}(t)] = U_{C1}(t) + \cdots \\ \qquad L_p \frac{dI_{Lp}(t)}{dt} - M \frac{dI_{Ls}(t)}{dt} \\ C_1 \frac{dU_{C1}(t)}{dt} = I_{Lp}(t) \\ L_s \frac{dI_{Ls}(t)}{dt} + U_{C2}(t) + g_D(t) U_{CF}(t) = M \frac{dI_{Lp}(t)}{dt} \\ C_2 \frac{dU_{C2}(t)}{dt} = I_{Ls}(t) \\ C_F \frac{dU_{CF}(t)}{dt} + \frac{U_{CF}(t)}{R_L} = g_D(t) I_{Ls}(t). \end{cases} \tag{22}$$

Equations (23)–(25) show the expressions of g_{Q1}, g_{Q2}, and g_D. $g_{Q1}(t) = 1$ means Q_1 is ON and Q_3 is OFF; $g_{Q1}(t) = 0$ indicates Q_1 is OFF and Q_3 is ON. Similarly, $g_{Q2}(t) = 1$ means Q_2 is ON and Q_4 is OFF; $g_{Q2}(t) = 0$ indicates Q_2 is OFF and Q_4 is ON. The rectifier works in the positive half cycle when $g_D(t) = 1$ and in the negative half cycle when $g_D(t) = -1$.

$$g_{Q1}(t) = \begin{cases} 1, mT \le t < (m+1-D)T, m \in N \\ 0, (m+1-D)T \le t < (m+1)T, m \in N \end{cases} \tag{23}$$

TABLE II
COMPARISON BETWEEN THE PROPOSED AND CONVENTIONAL MAGNETIC COUPLERS

Coupler	Planar circular	Planar square	DD	Proposed
Configuration	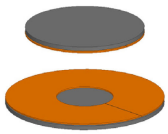	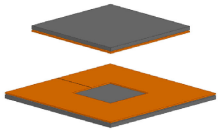	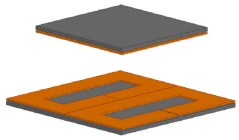	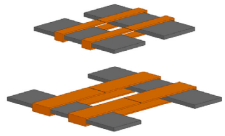
Coordinate system	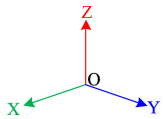	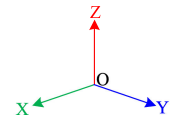	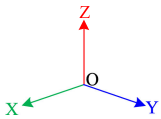	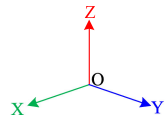
Coil size (mm)*	PS: 400/144 SS: 300/172	PS: 400×400/144×144 SS: 300×300/172×172	PS: (400×200/272×72)×2 SS: (300×150/236×86)×2	PS: (400×64+400×64)×2 SS: (300×32+300×32)×2
Ferrite size (mm)	PS: Φ400 SS: Φ300	PS: 400×400 SS: 300×300	PS: 400×400 SS: 300×300	PS: 400×100×2 SS: 300×112.5×2
PTD (mm)	170	170	170	170
k_{ali}	0.1266	0.1567	0.0845	0.1069
$k_{\Delta X=200}$	0.0215	0.0344	0.0404	0.0853
$k_{\Delta Y=100}$	0.0850	0.1126	0.0305	0.0778
$CRR_{\Delta X=200}$	0.170	0.220	0.478	0.798
$CRR_{\Delta Y=100}$	0.672	0.719	0.361	0.728

*Coil sizes of the planar circular, planar square, DD and proposed couplers are expressed in the following forms. Planar circular: outer diameter/inner diameter, planar square: outer side length × outer side width/inner side length × inner side width, DD: (outer side length × outer side width/inner side length × inner side width of a single D coil) × number of D coils, proposed: (length × width of the first part + length × width of the second part) × number of layers.

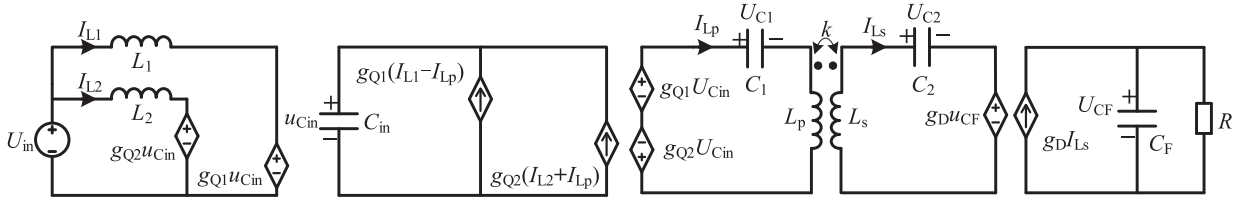

Fig. 18. Equivalent circuit diagram of the proposed system.

$$g_{Q2}(t)=\begin{cases}1, \left(m+\frac{1}{2}\right)\mathrm{T}\le t<\left(m+\frac{3}{2}-D\right)\mathrm{T}, m\in\mathrm{N}\\ 0, \left(m+\frac{3}{2}-D\right)\mathrm{T}\le t<\left(m+\frac{3}{2}\right)\mathrm{T}, m\in\mathrm{N}\end{cases} \tag{24}$$

$$g_{D}(t)=\begin{cases}1, \left(m-\frac{1}{4}\right)\mathrm{T}\le t<\left(m+\frac{1}{4}\right)\mathrm{T}, m\in\mathrm{N}\\ -1, \left(m+\frac{1}{4}\right)\mathrm{T}\le t<\left(m+\frac{3}{4}\right)\mathrm{T}, m\in\mathrm{N}.\end{cases} \tag{25}$$

The Fourier series coefficient of $g_{Q1}(t)$ is

$$\langle g_{Q1}(t)\rangle_k=\frac{1}{\mathrm{T}}\left(\int_{\mathrm{T}} g_{Q1}(t)\,e^{-\mathrm{j}k\omega t}\mathrm{d}t\right). \tag{26}$$

By expanding $\langle g_{Q1}(t)\rangle_k$ at $k=0$ and ±1, (27) can be yielded

$$\begin{cases}\langle g_{Q1}\rangle_0=1-D\\ \langle g_{Q1}\rangle_1=-\frac{1}{2\pi}\sin 2\pi D+\frac{\mathrm{j}}{2\pi}(\cos 2\pi D-1)\\ \langle g_{Q1}\rangle_{-1}=-\frac{1}{2\pi}\sin 2\pi D+\frac{\mathrm{j}}{2\pi}(1-\cos 2\pi D).\end{cases} \tag{27}$$

Similarly, (28) and (29) can be obtained by expanding $\langle g_{Q2}(t)\rangle_k$ and $\langle g_D(t)\rangle_k$ at $k=0$ and ±1

$$\begin{cases}\langle g_{Q2}\rangle_0=1-D\\ \langle g_{Q2}\rangle_1=\frac{1}{2\pi}\sin 2\pi D+\frac{\mathrm{j}}{2\pi}(1-\cos 2\pi D)\\ \langle g_{Q2}\rangle_{-1}=\frac{1}{2\pi}\sin 2\pi D+\frac{\mathrm{j}}{2\pi}(\cos 2\pi D-1)\end{cases} \tag{28}$$

$$\begin{cases}\langle g_{D}\rangle_0=0\\ \langle g_{D}\rangle_1=\frac{2}{\pi}\\ \langle g_{D}\rangle_{-1}=\frac{2}{\pi}.\end{cases} \tag{29}$$

As shown in (30), the variables in (22) can be approximated by their Fourier series. Both the –1, 0, and +1 order Fourier series of I_{L1}, I_{L2}, and U_{Cin} are considered because they contain both dc and ac components. By contrast, only the –1 and +1 order Fourier series of U_{C1}, U_{C2}, I_{Lp}, and I_{Ls} are taken into consideration since they are approximately sinusoidal. The ripple of U_{CF} is very small. Hence, only the 0 order Fourier series of U_{CF} is taken into account.

$$\begin{cases}I_{L1}(t)\approx\langle I_{L1}\rangle_{-1}e^{-\mathrm{j}\omega t}+\langle I_{L1}\rangle_0+\langle I_{L1}\rangle_1 e^{\mathrm{j}\omega t}\\ I_{L2}(t)\approx\langle I_{L2}\rangle_{-1}e^{-\mathrm{j}\omega t}+\langle I_{L2}\rangle_0+\langle I_{L2}\rangle_1 e^{\mathrm{j}\omega t}\\ U_{Cin}(t)\approx\langle U_{Cin}\rangle_{-1}e^{-\mathrm{j}\omega t}+\langle U_{Cin}\rangle_0+\langle U_{Cin}\rangle_1 e^{\mathrm{j}\omega t}\\ U_{C1}(t)\approx\langle U_{C1}\rangle_{-1}e^{-\mathrm{j}\omega t}+\langle U_{C1}\rangle_1 e^{\mathrm{j}\omega t}\\ I_{Lp}(t)\approx\langle I_{Lp}\rangle_{-1}e^{-\mathrm{j}\omega t}+\langle I_{Lp}\rangle_1 e^{\mathrm{j}\omega t}\\ I_{Ls}(t)\approx\langle I_{Ls}\rangle_{-1}e^{-\mathrm{j}\omega t}+\langle I_{Ls}\rangle_1 e^{\mathrm{j}\omega t}\\ U_{C2}(t)\approx\langle U_{C2}\rangle_{-1}e^{-\mathrm{j}\omega t}+\langle U_{C2}\rangle_1 e^{\mathrm{j}\omega t}\\ U_{CF}(t)\approx\langle U_{CF}\rangle_0.\end{cases} \tag{30}$$

The –1 and +1 order Fourier series coefficients are conjugate and symmetric. Therefore, we only need to solve the real and imaginary parts of the +1 order Fourier series coefficient. Then,

the real and imaginary parts of the –1 order Fourier series can be obtained, and the circuit variable can be restored using (30).

Let

$$\begin{cases} \langle I_{\mathrm{L1}}\rangle_0 = x_1, \langle I_{\mathrm{L1}}\rangle_1 = x_2 + \mathrm{j}x_3 \\ \langle I_{\mathrm{L2}}\rangle_0 = x_4, \langle I_{\mathrm{L2}}\rangle_1 = x_5 + \mathrm{j}x_6 \\ \langle U_{\mathrm{Cin}}\rangle_0 = x_7, \langle U_{\mathrm{Cin}}\rangle_1 = x_8 + \mathrm{j}x_9 \\ \langle U_{\mathrm{C1}}\rangle_1 = x_{10} + \mathrm{j}x_{11} \\ \langle I_{\mathrm{Lp}}\rangle_1 = x_{12} + \mathrm{j}x_{13} \\ \langle I_{\mathrm{Ls}}\rangle_1 = x_{14} + \mathrm{j}x_{15} \\ \langle U_{\mathrm{C2}}\rangle_1 = x_{16} + \mathrm{j}x_{17} \\ \langle U_{\mathrm{CF}}\rangle_0 = x_{18}. \end{cases} \tag{31}$$

The generalized state variables can be obtained as follows:

$$\mathbf{x}(t) = [x_1, x_2, \ldots, x_{18}]^T. \tag{32}$$

The product in (22) can be decoupled using the convolution property of Fourier series. Based on the differential and linear properties of the Fourier series, the differential equations of the system can be simplified as

$$\begin{cases} \dot{\mathbf{x}}(t) = \mathbf{A}\mathbf{x}(t) + \mathbf{B}\mathbf{u}(t) \\ \mathbf{y}(t) = \mathbf{C}\mathbf{x}(t) + \mathbf{D}\mathbf{u}(t) \end{cases} \tag{33}$$

where $\boldsymbol{u}(t) = [U_{\mathrm{in}}]$ is the input voltage of the system, and $\boldsymbol{y}(t) = [U_{\mathrm{O}}] = [U_{\mathrm{CF}}]$ is the output voltage of the system. $\boldsymbol{A}$ is a 18×18 matrix given in Appendix A. $\boldsymbol{B}$, $\boldsymbol{C}$, and $\boldsymbol{D}$ are shown in (34), (35), and (36), respectively. $\mathbf{Z}_{\mathrm{m\times n}}$ denotes an m×n zero matrix.

$$\mathbf{B} = \left[\tfrac{1}{L_1}\ \tfrac{1}{L_1}\ 0\ \tfrac{1}{L_2}\ \tfrac{1}{L_2}\ \mathbf{Z}_{1\times 15}\right]^{\mathrm{T}}_{1\times 18} \tag{34}$$

$$\mathbf{C} = \left[\mathbf{Z}_{1\times 17}\ 1\right]_{1\times 18} \tag{35}$$

$$\mathbf{D} = [0]. \tag{36}$$

The state variables in (33) do not change with time in steady state. Hence, their derivatives are 0, i.e., the left side of the equation is 0. Then, the steady-state solution of the system can be obtained

$$\begin{cases} \mathbf{X_{ss}} = -\mathbf{A}^{-1}\mathbf{B}\mathbf{U_{ss}} \\ \mathbf{Y_{ss}} = \mathbf{C}\mathbf{X_{ss}} + \mathbf{D}\mathbf{U_{ss}}. \end{cases} \tag{37}$$

Add a small disturbance to the state variables and input variable, i.e.,

$$\begin{cases} x_{\mathrm{i}} = X_{\mathrm{i,ss}} + \hat{x}_{\mathrm{i}}\ (i = 1, 2, \ldots 18) \\ U_{\mathrm{in}} = U_{\mathrm{in,ss}} + \hat{u}_{\mathrm{in}} \\ y = Y_{\mathrm{ss}} + \hat{y} \\ D = D_{\mathrm{ss}} + \hat{d}. \end{cases} \tag{38}$$

Substituting (38) into (33) and ignoring the steady-state variables and second-order small signal variables, the small signal model is finally acquired

$$\begin{cases} \dot{\hat{\mathbf{x}}}(\mathbf{t}) = \mathbf{A}\hat{\mathbf{x}}(\mathbf{t}) + \mathbf{B}\hat{\mathbf{u}}(\mathbf{t}) + \mathbf{E}\hat{\mathbf{d}}(\mathbf{t}) \\ \hat{\mathbf{y}}(\mathbf{t}) = \mathbf{C}\hat{\mathbf{x}}(\mathbf{t}) + \mathbf{D}\hat{\mathbf{u}}(\mathbf{t}). \end{cases} \tag{39}$$

The full expressions of $\boldsymbol{E}$ are given in Appendix B. In order to calculate the small signal transfer function from the duty cycle D to the output voltage U_{O}, it is assumed that the input voltage does not fluctuate, i.e.,

$$\hat{u}_{\mathrm{in}}(t) = 0. \tag{40}$$

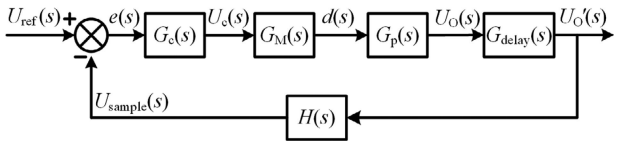

Fig. 19. Block diagram of the proposed closed-loop control system.

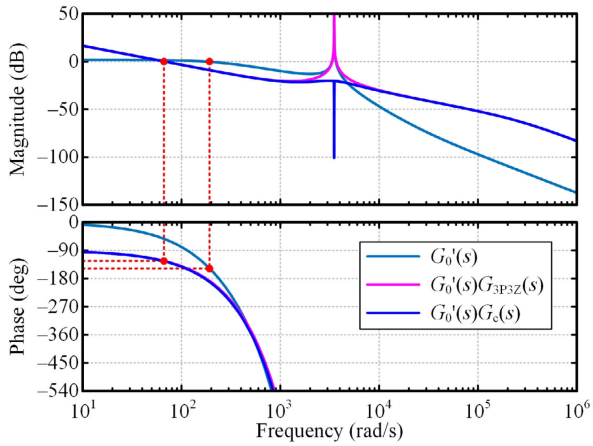

Fig. 20. Bode diagrams of $G_0'(s)$, $G_0'(s)G_{3\mathrm{P}3\mathrm{Z}}(s)$, and $G_0'(s)G_{\mathrm{c}}(s)$.

Then, the small signal transfer function of the system can be deduced as follows:

$$G_{\mathrm{p}}(s) = \frac{\hat{U}_O}{\hat{d}} = \mathbf{C}(\mathbf{sI} - \mathbf{A})^{-1}\mathbf{E}. \tag{41}$$

B. Design of the Closed-Loop Controller

Fig. 19 shows the block diagram of the proposed closed loop control system, where $G_{\mathrm{c}}(s)$, $G_{\mathrm{M}}(s)$, $G_{\mathrm{p}}(s)$, $G_{\mathrm{delay}}(s)$, and $H(s)$ are the transfer functions of the compensator, PWM modulator, WPT system, wireless communication delay, and voltage sampling, respectively.

The gain function of the uncompensated system is

$$G_0(s) = G_{\mathrm{M}}(s)G_{\mathrm{p}}(s)G_{\mathrm{delay}}(s)H(s). \tag{42}$$

The maximum delay of the wireless communication module (Bluetooth in this article) is 10 ms. Hence, $G_{\mathrm{delay}}(s)$ can be expressed as follows:

$$G_{\mathrm{delay}}(s) = e^{-0.01s}. \tag{43}$$

The Bode diagram of $G_0(s)$ has 17 poles and 15 zeros. It is too complicated to be analyzed and most poles and zeros have little impact on the closed loop control. Hence, a simplified gain function $G_0'(s)$ is derived where only the dominant poles and zeros are preserved and the other poles and zeros are removed. When the transmitter and receiver are aligned (the coupling coefficient equals 0.112), the expression of $G_0'(s)$ is given by (44), based on which the Bode diagram is plotted and shown in

Fig. 20

$$G_0{}'(s) = \frac{1.234 \times \left(\frac{1}{27729}s+1\right) \times e^{-0.01s}}{\left(\frac{1}{247.19}s+1\right) \times \left(\frac{1}{3508.7^2}s^2+5.37\times10^{-8}s+1\right)}. \tag{44}$$

From Fig. 20, the phase margin of the uncompensated system is 26°, less than 30°. Besides, the low-frequency gain of the system is low, indicating a relatively large steady-state error. Hence, the system must be compensated. Considering the communication delay, the sheared frequency should be quite low to obtain sufficient phase margin. Three-pole and three-zero (3P3Z) compensator is finally selected, and the gain function of the compensated system is given by (45)

$$G_{3P3Z}(s) = \frac{55 \times \left(\frac{1}{247.19}s+1\right) \times \left(\frac{1}{1754}s+1\right)^2}{s \times \left(\frac{1}{27729}s+1\right) \times \left(\frac{1}{85\times10^3\pi}s+1\right)}. \tag{45}$$

The Bode diagram of the system after adding $G_{3P3Z}(s)$ is also plotted in Fig. 20. The amplitude-frequency curve crosses the 0 dB line twice near 3508.7 rad/s, which could affect the stability of the system. Hence, a band-stop filter is added at this angular frequency. The transfer function of the band-stop filter is given by (46)

$$G_{BSF}(s) = \frac{s^2+3508.7^2}{s^2+3508.7s+3508.7^2}. \tag{46}$$

According to the previous analysis, the compensator $G_c(s)$ consists of two parts—the 3P3Z compensator $G_{3P3Z}(s)$, and the band-stop filter $G_{BSF}(s)$. Hence,

$$G_c(s) = G_{3P3Z}(s)\, G_{BSF}(s). \tag{47}$$

In order to conveniently see the changes of the Bode diagrams with and without the band-stop filter, the Bode diagram of the system after adding $G_c(s)$ is shown in Fig. 20 as well. The phase margin is 54.4° and the sheared frequency is 68 rad/s. The low-frequency gain of the system is significantly increased, reducing the steady-state error. The amplitude-frequency curve crosses the 0 dB line with a slope of –20 dB/dec. The stability of the system is improved. In addition, it decreases at a slope of –40 dB/dec in the high-frequency band. Hence, the high-frequency ripple can be signicantly suppressed.

When the receiver deviates from the aligned position to the maximum misaligned position (the coupling coefficient decreases from 0.112 to 0.081), the phase margin decreases from 54.4° to 40.5°, while the sheared frequency increases from 68 to 94.1 rad/s. The other characteristics of the system are similar to those under the aligned case. Hence, the proposed system can run stably in the whole operation area.

Based on (45) to (47), the differential algorithm of the digital compensator can be obtained using the bilinear transformation method

$$\begin{aligned} u_c(k) = {} & 3.46u_c(k-1) - 4.23u_c(k-2) + 1.94u_c(k-3) \\ & - 0.01u_c(k-4) - 0.15u_c(k-5) + 179.38e(k) \\ & - 888.73e(k-1) + 1761.56e(k-2) \\ & - 1746.07e(k-3) + 865.48e(k-4) \\ & - 171.62e(k-5) \end{aligned} \tag{48}$$

where $u_c(k)$ is the output voltage of the compensator at the instant of kth sampling, and $e(k)$ represents the error between the sampling voltage and reference, also at the instant of the kth sampling.

TABLE III
KEY REQUIREMENTS OF THE PROTOTYPE

Parameter	Symbol	Value
DC input voltage	U_{in}	100 V
Output voltage	U_O	100 V
Nominal output power	P_N	500 W
Power transfer distance	D_{PT}	170 mm
Maximum X-direction misalignment	ΔX_{max}	200 mm
Maximum Y-direction misalignment	ΔY_{max}	100 mm

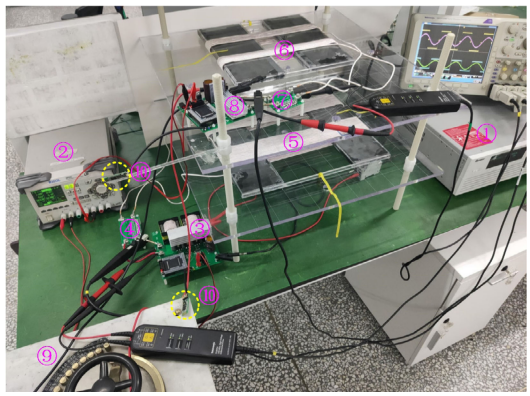

Fig. 21. Prototype for electric vehicle wireless charging.

V. SYSTEM DESIGN AND EXPERIMENT VERIFICATION

A prototype was built to verify the correctness of the theoretical analysis and the advantages of the proposed EVWCS. The key requirements of the prototype are listed in Table III. The numbers of turns of the transmitter and receiver are 40 and 20, respectively, and the specification of the employed Litz wire is Φ0.1 mm × 500.

Fig. 21 shows the prototype comprised of ten modules as follows:

1) a dc voltage source for the power circuit;
2) a dc voltage source for the driver and controller;
3) a boost inverter;
4) a primary compensation capacitor;
5) a transmitter;
6) a receiver;
7) a secondary compensation capacitor;
8) a full-bridge rectifier and a sampling circuit;
9) a resistive load;

TABLE IV
KEY PARAMETERS UTILIZED IN THE PROTOTYPE

Parameter	Value/Type	Parameter	Value/Type
f_0	85 kHz	L_P	1090.4 μH
C_{in}	100 μF/450 V	L_S	258.9 μH
$Q_1 - Q_4$	STW70N60DM2	C_1	3.22 nF
L_1	404.4 μH	C_2	13.5 nF
L_2	406.6 μH	$D_1 - D_4$	MBR40200WT
k_{ali}	0.112	C_F	200 μF/450 V
$k_{AX=200}$	0.090	R_N	20 Ω
$k_{AY=100}$	0.081	Bluetooth	HC-05

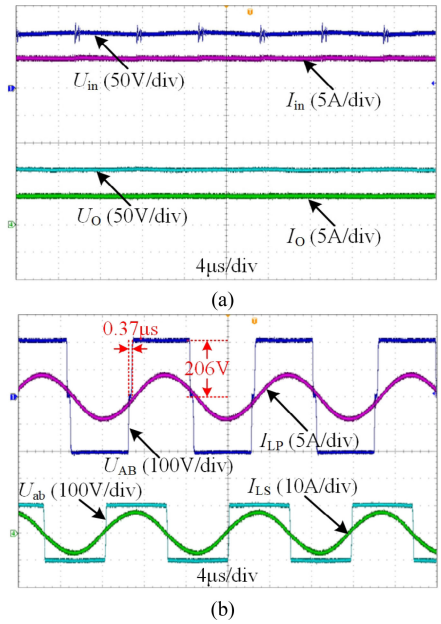

Fig. 22. Voltages and currents across each power stage of the prototype in aligned case.

10) two bluetooth modules surrounded by yellow dashed circles.

The key parameters utilized in the prototype are listed in Table IV.

The voltages and currents across each power stage of the prototype in aligned case are shown in Fig. 22. The output voltage U_O is 100 V, exactly equal to the designed value. The input and output power are 555 and 500 W, respectively, indicating a power transfer efficiency (PTE) of 90.1%. From Fig. 22(b), the dead time is 0.37 μs. Hence, θ_{dead} is 0.03146π and the duty cycle is 0.5157. U_{Cin} is boosted to 206 V.

The prototype was also tested when $\Delta X = 200$ mm and $\Delta Y = 100$ mm. The voltage and current waveforms in these two cases are similar to those shown in Fig. 22. For the sake of brevity, they are not shown here. The measured U_O are 99.8 and 100 V in these two cases, respectively, which are very close to or exactly equal to the designed value, validating the effectiveness of the closed-loop control. Owing to the drops of the coupling coefficients, the PTEs in these two cases decrease to 86.2% and 87.0%, respectively. This can be qualitatively explained as follows. In terms of (5) and (12), U_{AB1} should decrease to keep U_O constant when k is decreased. The decrease of U_{AB1} results in a larger current flowing through C_1 and L_P and more loss. The duty cycles in the aforementioned two cases are 0.4728 and 0.4715, and U_{Cin} are boosted into 185 and 183 V, respectively.

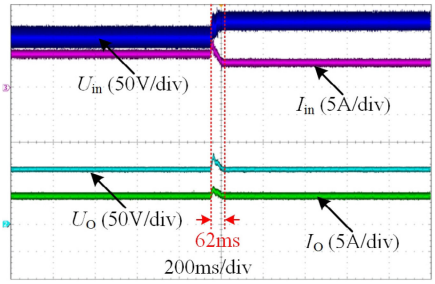

Fig. 23. Dynamic response of the prototype under aligned case.

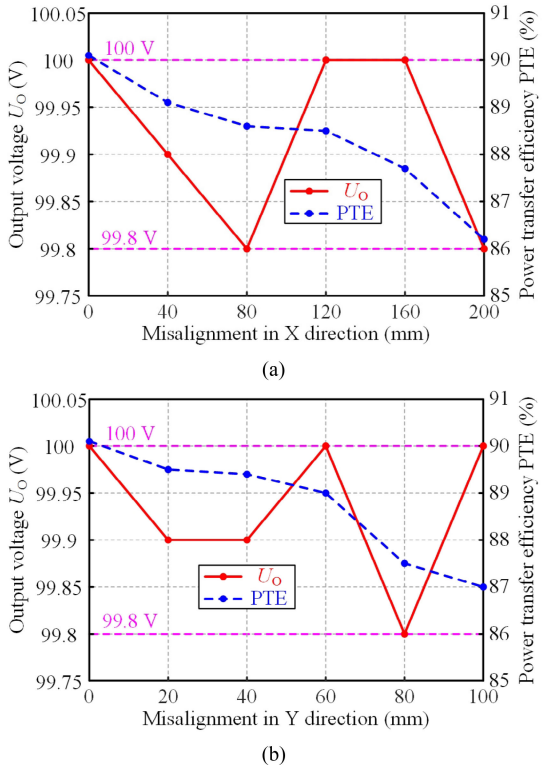

Fig. 24. Plots of the output voltages and PTEs versus (a) X- and (b) Y-direction misalignment.

Fig. 23 shows the dynamic response of the prototype when U_{in} increases from 90 to 120 V under aligned case. The setting time is 62 ms. The dynamic performance of the prototype is quite good because many inductors and capacitors exist in the system. This experiment further verifies the effectiveness of the closed-loop control.

Fig. 24 shows the plots of output voltages and PTEs versus misalignments in both *X* and *Y* directions. In the whole operating area, the output voltage is stable which only fluctuates by 0.2%. The accuracy of the closed-loop control is demonstrated. PTE decreases when *X*- and *Y*-direction misalignments are increased. However, the minimum PTE is as high as 86.2% even if the *X*-direction misalignment is 200 mm. More importantly, such

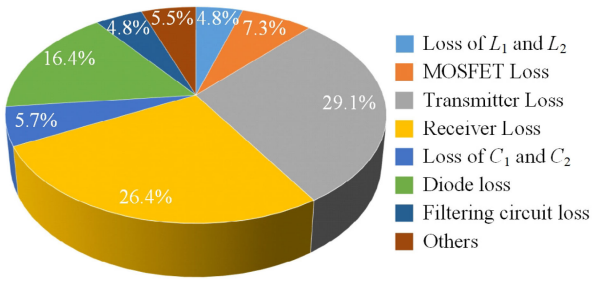

Fig. 25. Loss distribution of the prototype in aligned case.

efficiency is achieved in the case that the employed ferrite is reduced by 41% and the power transfer distance is as long as 170 mm.

The loss distribution of the prototype in aligned case is shown in Fig. 25. The transmitter loss is the highest among all losses. This agrees well with the analysis in Section II-C and verifies the advantages of using a boost inverter in an EVWCS. The receiver loss ranks the second place among all losses because of relatively large current and ESR. The diode loss accounts for 16.4% of the total loss. Synchronous rectification will be employed to reduce the diode loss. The loss of L_1 and L_2 are quite small. Hence, the introduction of these two inductors will not significantly reduce system efficiency.

VI. Conclusion

This article proposes an EVWCS using a BI and an optimized FSC. The BI has three advantages than the conventional FBI. First, it results in a higher dc bus voltage and lower transmitter current. Hence, the power loss is reduced. Next, the interleaved structure of a BI effectively reduces the input current ripple. The interference from the EVWCS to the power grid is diminished. Third, the BI has wider adjustment range than the FBI, which means a larger parameter variation range is allowed. The system using BI offers greater operating freedom. This article also proposes a parameter design method for FSCs. Double-I-shaped core performs best providing that the removed ferrite is constant. Separation of the windings can further increase the coupling coefficient. A 500-W prototype was built. The variation of the output voltage is no more than 0.2 V in the whole operating area. A highest PTE of 90.1% is achieved even if the ferrite is removed by 41% and the power transfer distance is 170 mm.

Appendix A

The coefficient matrix $\boldsymbol{A}$ is divided into 36 three-row–three-column submatrices. The nonzero submatrices are given as follows, where $\Delta = M^2 - L_p L_s$:

$$\boldsymbol{A} = \begin{bmatrix} \boldsymbol{A}_{11} & \boldsymbol{Z}_{3\times3} & \boldsymbol{A}_{13} & \boldsymbol{Z}_{3\times3} & \boldsymbol{Z}_{3\times3} & \boldsymbol{Z}_{3\times3} \\ \boldsymbol{Z}_{3\times3} & \boldsymbol{A}_{22} & \boldsymbol{A}_{23} & \boldsymbol{Z}_{3\times3} & \boldsymbol{Z}_{3\times3} & \boldsymbol{Z}_{3\times3} \\ \boldsymbol{A}_{31} & \boldsymbol{A}_{32} & \boldsymbol{A}_{33} & \boldsymbol{A}_{34} & \boldsymbol{A}_{35} & \boldsymbol{Z}_{3\times3} \\ \boldsymbol{Z}_{3\times3} & \boldsymbol{Z}_{3\times3} & \boldsymbol{A}_{43} & \boldsymbol{A}_{44} & \boldsymbol{A}_{45} & \boldsymbol{A}_{46} \\ \boldsymbol{Z}_{3\times3} & \boldsymbol{Z}_{3\times3} & \boldsymbol{A}_{53} & \boldsymbol{A}_{54} & \boldsymbol{A}_{55} & \boldsymbol{A}_{56} \\ \boldsymbol{Z}_{3\times3} & \boldsymbol{Z}_{3\times3} & \boldsymbol{Z}_{3\times3} & \boldsymbol{Z}_{3\times3} & \boldsymbol{A}_{65} & \boldsymbol{A}_{66} \end{bmatrix}$$

$$\boldsymbol{A}_{11} = \boldsymbol{A}_{22} = \boldsymbol{A}_{33} = \boldsymbol{A}_{55} = \begin{bmatrix} 0 & 0 & 0 \\ 0 & 0 & \omega \\ 0 & -\omega & 0 \end{bmatrix}$$

$$\boldsymbol{A}_{13} = \begin{bmatrix} \frac{D-1}{L_1} & \frac{\sin 2\pi D}{L_1\pi} & \frac{1-cos2\pi D}{L_1\pi} \\ \frac{\sin 2\pi D}{2L_1\pi} & \frac{D-1}{L_1} & 0 \\ \frac{1-cos2\pi D}{2L_1\pi} & 0 & \frac{D-1}{L_1} \end{bmatrix}$$

$$\boldsymbol{A}_{23} = \begin{bmatrix} \frac{D-1}{L_2} & \frac{-\sin 2\pi D}{L_2\pi} & \frac{cos2\pi D-1}{L_2\pi} \\ \frac{-\sin 2\pi D}{2L_2\pi} & \frac{D-1}{L_2} & 0 \\ \frac{cos2\pi D-1}{2L_2\pi} & 0 & \frac{D-1}{L_2} \end{bmatrix}$$

$$\boldsymbol{A}_{31} = \begin{bmatrix} \frac{1-D}{C_{\text{in}}} & \frac{-\sin 2\pi D}{C_{\text{in}}\pi} & \frac{cos2\pi D-1}{C_{\text{in}}\pi} \\ \frac{-\sin 2\pi D}{2C_{\text{in}}\pi} & \frac{1-D}{C_{\text{in}}} & 0 \\ \frac{cos2\pi D-1}{2C_{\text{in}}\pi} & 0 & \frac{1-D}{C_{\text{in}}} \end{bmatrix}$$

$$\boldsymbol{A}_{32} = \begin{bmatrix} \frac{1-D}{C_{\text{in}}} & \frac{\sin 2\pi D}{C_{\text{in}}\pi} & \frac{1-cos2\pi D}{C_{\text{in}}\pi} \\ \frac{\sin 2\pi D}{2C_{\text{in}}\pi} & \frac{1-D}{C_{\text{in}}} & 0 \\ \frac{1-cos2\pi D}{2C_{\text{in}}\pi} & 0 & \frac{1-D}{C_{\text{in}}} \end{bmatrix}$$

$$\boldsymbol{A}_{34} = \begin{bmatrix} 0 & 0 & 2\sin 2\pi D/(C_{\text{in}}\pi) \\ 0 & 0 & 0 \\ 0 & 0 & 0 \end{bmatrix}$$

$$\boldsymbol{A}_{35} = \begin{bmatrix} 2\,(1-cos2\pi D)/(C_{\text{in}}\pi) & 0 & 0 \\ 0 & 0 & 0 \\ 0 & 0 & 0 \end{bmatrix}$$

$$\boldsymbol{A}_{43} = \begin{bmatrix} 0 & 0 & 0 \\ 0 & 0 & 0 \\ L_{\text{s}}\sin 2\pi D/(\pi\Delta) & 0 & 0 \end{bmatrix}$$

$$\boldsymbol{A}_{44} = \begin{bmatrix} 0 & \omega & 1/C_1 \\ -\omega & 0 & 0 \\ L_{\text{s}}/\Delta & 0 & 0 \end{bmatrix}$$

$$\boldsymbol{A}_{45} = \begin{bmatrix} 0 & 0 & 0 \\ 1/C_1 & 0 & 0 \\ \omega & 0 & 0 \end{bmatrix}, \quad \boldsymbol{A}_{46} = \begin{bmatrix} 0 & 0 & 0 \\ 0 & 0 & 0 \\ M/\Delta & 0 & 2M/(\pi\Delta) \end{bmatrix}$$

$$\boldsymbol{A}_{53} = \begin{bmatrix} L_{\text{s}}(1-\cos 2\pi D)/(\pi\Delta) & 0 & 0 \\ M\sin 2\pi D/(\pi\Delta) & 0 & 0 \\ M(1-\cos 2\pi D)/(\pi\Delta) & 0 & 0 \end{bmatrix}$$

$$\boldsymbol{A}_{54} = \begin{bmatrix} 0 & L_{\text{s}}/\Delta & -\omega \\ M/\Delta & 0 & 0 \\ 0 & M/\Delta & 0 \end{bmatrix}$$

$$\boldsymbol{A}_{56} = \begin{bmatrix} 0 & M/\Delta & 0 \\ L_{\text{p}}/\Delta & 0 & 2L_{\text{p}}/(\pi\Delta) \\ 0 & L_{\text{p}}/\Delta & 0 \end{bmatrix}$$

$$\boldsymbol{A}_{65} = \begin{bmatrix} 0 & 1/C_2 & 0 \\ 0 & 0 & 1/C_2 \\ 0 & 4/(\pi C_{\text{F}}) & 0 \end{bmatrix}$$

$$\boldsymbol{A}_{66} = \begin{bmatrix} 0 & \omega & 0 \\ -\omega & 0 & 0 \\ 0 & 0 & -1/(C_{\text{F}}R) \end{bmatrix}.$$

APPENDIX B

$$\mathbf{E}=\begin{bmatrix}
\frac{X_{7,\mathrm{ss}}}{L_1}+\frac{2\cos 2\pi D}{L_1}X_{8,\mathrm{ss}}+\frac{2\sin 2\pi D}{L_1}X_{9,\mathrm{ss}} \\
\frac{\cos 2\pi D}{L_1}X_{7,\mathrm{ss}}+\frac{X_{8,\mathrm{ss}}}{L_1} \\
\frac{\sin 2\pi D}{L_1}X_{7,\mathrm{ss}}+\frac{X_{9,\mathrm{ss}}}{L_1} \\
\frac{X_{7,\mathrm{ss}}}{L_2}-\frac{2\cos 2\pi D}{L_2}X_{8,\mathrm{ss}}+\frac{2\sin 2\pi D}{L_2}X_{9,\mathrm{ss}} \\
\frac{-\cos 2\pi D}{L_2}X_{7,\mathrm{ss}}+\frac{X_{8,\mathrm{ss}}}{L_2} \\
\frac{-\sin 2\pi D}{L_2}X_{7,\mathrm{ss}}+\frac{X_{9,\mathrm{ss}}}{L_2} \\
\begin{pmatrix}
\frac{-X_{1,\mathrm{ss}}}{C_{\mathrm{in}}}-\frac{2\cos 2\pi D}{C_{\mathrm{in}}}X_{2,\mathrm{ss}}-\frac{2\sin 2\pi D}{C_{\mathrm{in}}}X_{3,\mathrm{ss}}- \\
\frac{X_{4,\mathrm{ss}}}{C_{\mathrm{in}}}+\frac{2\cos 2\pi D}{C_{\mathrm{in}}}X_{5,\mathrm{ss}}+\frac{2\sin 2\pi D}{C_{\mathrm{in}}}X_{6,\mathrm{ss}}+ \\
\frac{4\cos 2\pi D}{C_{\mathrm{in}}}X_{12,\mathrm{ss}}-\frac{4\sin 2\pi D}{C_{\mathrm{in}}}X_{13,\mathrm{ss}}
\end{pmatrix} \\
\frac{-\cos 2\pi D}{C_{\mathrm{in}}}X_{1,\mathrm{ss}}-\frac{X_{2,\mathrm{ss}}}{C_{\mathrm{in}}}+\frac{\cos 2\pi D}{C_{\mathrm{in}}}X_{4,\mathrm{ss}}-\frac{X_{5,\mathrm{ss}}}{C_{\mathrm{in}}} \\
\frac{-\sin 2\pi D}{C_{\mathrm{in}}}X_{1,\mathrm{ss}}-\frac{X_{3,\mathrm{ss}}}{C_{\mathrm{in}}}+\frac{\sin 2\pi D}{C_{\mathrm{in}}}X_{4,\mathrm{ss}}-\frac{X_{6,\mathrm{ss}}}{C_{\mathrm{in}}} \\
\mathbf{Z}_{2\times 1} \\
\frac{2L_{\mathrm{s}}\cos 2\pi D}{\Delta}X_{7,\mathrm{ss}} \\
\frac{2L_{\mathrm{s}}\sin 2\pi D}{\Delta}X_{7,\mathrm{ss}} \\
\frac{2M\cos 2\pi D}{\Delta}X_{7,\mathrm{ss}} \\
\frac{2M\sin 2\pi D}{\Delta}X_{7,\mathrm{ss}} \\
\mathbf{Z}_{3\times 1}
\end{bmatrix}_{18\times 1}.$$

REFERENCES

[1] Z. Zhang, H. Pang, A. Georgiadis, and C. Cecati, "Wireless power transfer—An overview," *IEEE Trans. Ind. Electron.*, vol. 66, no. 2, pp. 1044–1058, Feb. 2019.

[2] F. Liu, Y. Yang, D. Jiang, X. Ruan, and X. Chen, "Modeling and optimization of magnetically coupled resonant wireless power transfer system with varying spatial scales," *IEEE Trans. Power Electron.*, vol. 32, no. 4, pp. 3240–3250, Apr. 2017.

[3] Z. Zhang, W. Ai, Z. Liang, and J. Wang, "Topology-reconfigurable capacitor matrix for encrypted dynamic wireless charging of electric vehicles," *IEEE Trans. Veh. Technol.*, vol. 67, no. 10, pp. 9284–9293, Oct. 2018.

[4] Z. Li, C. Zhu, J. Jiang, K. Song, and G. Wei, "A 3-kW wireless power transfer system for sightseeing car supercapacitor charge," *IEEE Trans. Power Electron.*, vol. 32, no. 5, pp. 3301–3316, May 2017.

[5] T. Kan, R. Mai, P. P. Mercier, and C. C. Mi, "Design and analysis of a three-phase wireless charging system for lightweight autonomous underwater vehicles," *IEEE Trans. Power Electron.*, vol. 33, no. 8, pp. 6622–6632, Aug. 2018.

[6] H. Liu, Q. Shao, and X. Fang, "Modeling and optimization of class-E amplifier at subnominal condition in a wireless power transfer system for biomedical implants," *IEEE Trans. Biomed. Circuits Syst.*, vol. 11, no. 1, pp. 35–43, Feb. 2017.

[7] U. K. Madawala and D. J. Thrimawithana, "New technique for inductive power transfer using a single controller," *IET Power Electron.*, vol. 5, no. 2, pp. 248–256, Feb. 2012.

[8] W. Jiang, J. Lai, and K. Hwu, "Digital compensator design for high-frequency hybrid resonant buck converter," in *7th Int. Symp. Next Gener. Electron.*, 2018, pp. 1–4.

[9] C. Zheng *et al.*, "High-efficiency contactless power transfer system for electric vehicle battery charging application," *IEEE J. Emerg. Sel. Topics Power Electron.*, vol. 3, no. 1, pp. 65–74, Mar. 2015.

[10] H. Hao, G. A. Covic, and J. T. Boys, "An approximate dynamic model of LCL-T-based inductive power transfer power supplies," *IEEE Trans. Power Electron.*, vol. 29, no. 10, pp. 5554–5567, Oct. 2014.

[11] Y. Yao, Y. Wang, X. Liu, Y. Pei, D. Xu, and X. Liu, "Particle swarm optimization-based parameter design method for S/CLC-compensated IPT systems featuring high tolerance to misalignment and load variation," *IEEE Trans. Power Electron.*, vol. 34, no. 6, pp. 5268–5282, Jun. 2019.

[12] Y. Wang, Y. Yao, X. Liu, D. Xu, and L. Cai, "An LC/S compensation topology and coil design technique for wireless power transfer," *IEEE Trans. Power Electron.*, vol. 33, no. 3, pp. 2007–2025, Mar. 2018.

[13] H. Feng, T. Cai, S. Duan, J. Zhao, X. Zhang, and C. Chen, "An LCC-compensated resonant converter optimized for robust reaction to large coupling variation in dynamic wireless power transfer," *IEEE Trans. Ind. Electron.*, vol. 63, no. 10, pp. 6591–6601, Oct. 2016.

[14] J. Hou, Q. Chen, X. Ren, X. Ruan, S. Wong, and C. K. Tse, "Precise characteristics analysis of series/series-parallel compensated contactless resonant converter," *IEEE J. Emerg. Sel. Topics Power Electron.*, vol. 3, no. 1, pp. 101–110, Mar. 2015.

[15] Y. Yao, Y. Wang, X. Liu, F. Lin, and D. Xu, "A novel parameter tuning method for a double-sided LCL compensated WPT system with better comprehensive performance," *IEEE Trans. Power Electron.*, vol. 33, no. 10, pp. 8525–8536, Oct. 2018.

[16] M. Chigira, Y. Nagatsuka, Y. Kaneko, S. Abe, T. Yasuda, and A. Suzuki, "Small-size light-weight transformer with new core structure for contactless electric vehicle power transfer system," *IEEE Energy Convers. Congr. Expo.*, 2011, pp. 260–266.

[17] H. Takanashi, Y. Sato, Y. Kaneko, S. Abe, and T. Yasuda, "A large air gap 3 kW wireless power transfer system for electric vehicles," *IEEE Energy Convers. Congr. Expo.*, 2012, pp. 269–274.

[18] T. Fujita, T. Yasuda, and H. Akagi, "A wireless power transfer system with a double-current rectifier for EVs," in *Proc. IEEE Energy Convers. Congr. Expo.*, 2016, pp. 1–7.

[19] G. Yang, S. Dong, C. Zhu, R. Lu, G. Wei, and K. Song, "Design of a high lateral misalignment tolerance magnetic coupler for wireless power transfer systems," in *Proc. IEEE PELS Workshop Emerg. Technol.: Wireless Power Transfer*, 2017, pp. 34–39.

[20] Y. Tang, F. Zhu, Y. Wang, and H. Ma, "Design and optimizations of solenoid magnetic structure for inductive power transfer in EV applications," in *Proc. 41st Annu. Conf. IEEE Ind. Electron. Soc.*, 2015, pp. 001459–001464.

[21] Y. Nagatsuka, N. Ehara, Y. Kaneko, S. Abe, and T. Yasuda, "Compact contactless power transfer system for electric vehicles," in *Proc. Int. Power Electron. Conf.*, 2010, pp. 807–813.

[22] M. Budhia, G. Covic, and J. Boys, "A new IPT magnetic coupler for electric vehicle charging systems," in *Proc. 36th Annu. Conf. IEEE Ind. Electron. Soc.*, 2010, pp. 2487–2492.

[23] F. Zhao, G. Wei, C. Zhu, and K. Song, "Design and optimizations of asymmetric solenoid type magnetic coupler in wireless charging system for electric vehicles," in *Proc. IEEE PELS Workshop Emerg. Technol.: Wireless Power Transfer*, 2017, pp. 157–162.

[24] A. Tejeda, S. Kim, F. Y. Lin, G. A. Covic, and J. T. Boys, "A hybrid solenoid coupler for wireless charging applications," *IEEE Trans. Power Electron.*, vol. 34, no. 6, pp. 5632–5645, Jun. 2019.

Yousu Yao (Member, IEEE) was born in Jiangsu Province, China, in 1991. He received the B.S. and Ph.D. degrees in electrical engineering from the Harbin Institute of Technology, Harbin, China, in 2014 and 2019, respectively.

He is currently an Associate Professor with the School of Electrical Engineering and Automation, Harbin Institute of Technology, Harbin, China. He has authored/coauthored more than 40 journal and conference papers and holds seven patents. His research interests include wireless power transfer, dc–dc converter, magnetic coupler design, and simultaneous wireless power and data transfer.

Dr. Yao was the recipient of the First Prize Paper Award from the IEEE TRANSACTIONS ON POWER ELECTRONICS, and the Best Paper Awards from ICEMS 2019, SPEED 2019, and ITEC Asia-Pacific 2017.

Shenghan Gao was born in Suihua, Heilongjiang, China, in 1998. He received the B.S. degree in electrical engineering in 2019 from he Harbin Institute of Technology, Harbin, China, where he is currently working toward the M.S. degree in electrical engineering.

His research interests include wireless power transfer, magnetic coupling structure design, and digital control of dc–dc converters.

Yijie Wang (Senior member, IEEE) was born in Heilongjiang Province, China, in 1982. He received the B.S., M.S., and PH.D. degrees in electrical engineering from the Harbin Institute of Technology, Harbin, China, in 2005, 2007, and 2012, respectively.

From 2012 to 2014, he was a Lecturer with the Department of Electrical and Electronics Engineering, Harbin Institute of Technology. From 2014 to 2017, he was an Associate Professor with the Department of Electrical and Electronics Engineering, Harbin Institute of Technology. Since 2017, he has been a Professor with the Department of Electrical and Electronics Engineering, Harbin Institute of Technology. His research interests include dc–dc converters, soft-switching power converters, power factor correction circuits, digital control electronic ballasts, LED lighting systems.

Dr. Wang is an Associate Editor for the IEEE TRANSACTIONS ON INDUSTRIAL ELECTRONICS, the IEEE JOURNAL OF EMERGING AND SELECTED TOPICS IN POWER ELECTRONICS, the IEEE ACCESS, the *IET Power Electronics,* and the *Journal of Power Electronics*.

Xiaosheng Liu (Member, IEEE) was born in Qiqihar, Heilongjiang, China, in 1966. He received the B.S. and M.S. degrees in electrical engineering, and the Ph.D. degree in mechatronics engineering from Harbin Institute of Technology, Harbin, China, in 1988, 1993, and 1999, respectively.

He has been a Professor with the Department of Electrical Engineering, Harbin Institute of Technology, since 2006. His research interests include power line communication and its routing methods, communication networks and control technology, and information and communication of smart grids.

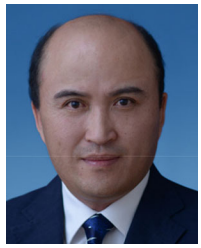

Xiangjun Zhang was born in Shandong Province, China, in 1971. He received the B.S. degree in welding from Xi'an Jiaotong University, Xi'an, China, in 1993, the M.S. degree in welding from Harbin Welding Institute, Harbin, China, in 1999, and the Ph.D. degree in electrical engineering from the Harbin Institute of Technology, Harbin, China, in 2006.

From 2006 to 2013, he was a Lecturer with the Department of Electrical and Electronics Engineering, Harbin Institute of Technology, where he has been an Associate Professor, since 2013. His research interests include the areas of electronic ballast, power factor correction circuits, high-power converters, and light emitting diode lighting systems.

Dianguo Xu (Fellow, IEEE) received the B.S. degree in control engineering from Harbin Engineering University, Harbin, China, in 1982, and the M.S. and Ph.D. degrees in electrical engineering from the Harbin Institute of Technology (HIT), Harbin, China, in 1984 and 1989 respectively.

In 1984, he was with the Department of Electrical Engineering, HIT, as an Assistant Professor. Since 1994, he has been a Professor with the Department of Electrical Engineering, HIT. He was the Dean with the School of Electrical Engineering and Automation, HIT, from 2000 to 2010. He is currently a Vice President with HIT. He has authored/coauthored more than 600 technical papers. His research interests include renewable energy generation technology, power quality mitigation, sensorless vector controlled motor drives, and high-performance PMSM servo system.

Dr. Xu is an Associate Editor for the IEEE TRANSACTIONS ON INDUSTRIAL ELECTRONICS, the IEEE TRANSACTIONS ON POWER ELECTRONICS, and the IEEE JOURNAL OF EMERGING AND SELECTED TOPICS IN POWER ELECTRONICS. He serves as a Chairman of the IEEE Harbin Section. He was the recipient of the 2018 IEEE Industry Applications Society Outstanding Achievement Award.